

Supplementary Information

NHC-Mediated Photocatalytic *Para*-Selective C-H Acylation of Aryl Alcohols: Regioselectivity Control via Remote Radical Spiro Cyclization

Tinglei Zhang,^{[a][e]} Lala Wang,^[a] Xiaolin Peng,^[a] Tianhui Liao,^[a] Dongmei Chen,^[a] Ting Tu,^[a] Donghan Liu,^[a] Ziyue Cheng,^[a] Shiqing Huang^[b], Shi-Chao Ren^{*[a]}, Xinglong Zhang^{*[c][d]}, and Yonggui Robin Chi^{*[a][b]}

^a State Key Laboratory of Green Pesticide; Key Laboratory of Green Pesticide and Agricultural Bioengineering, Ministry of Education, Center for R&D of Fine Chemicals of Guizhou University, Guiyang, 550025, China.

^b School of Chemistry, Chemical Engineering, and Biotechnology, Nanyang Technological University, Singapore 637371, Singapore.

^c Department of Chemistry, The Chinese University of Hong Kong, Shatin, New Territories, Hong Kong, China.

^d Institute of High Performance Computing, Agency for Science, Technology and Research, 1 Fusionopolis Way, #16-16 Connexis, Singapore, 138632, Singapore.

^e Qiannan Medical College for Nationalities, Duyun, 558003, P. R. China

E-mails: sren@gzu.edu.cn;

xinglong.zhang@cuhk.edu.hk

robinchi@ntu.edu.sg

Table of Contents

1	Supplementary Notes	S3
2	Supplementary Discussion	S4
	2.1 Condition optimizations	S4
3	Supplementary Methods	S5
	3.1 General procedure for the <i>para</i>-selective acylation reactions	S5
	3.2 General procedure for preparation of α-amido-oxy acid	S7
	3.3 General procedure for the synthesis of acyl imidazole salts	S8
	3.4 Procedure for the synthesis of dimethomorph analogue	S8
	3.5 Procedure for the synthesis of 10	S10
	3.6 Catalytic version of <i>para</i>-selective acylation reactions	S10
	3.7 TEMPO inhibition reaction	S11
	3.8 Intramolecular cyclization reaction	S11
	3.9 Stern-Volmer quenching experiments of PC-2	S12
4	X-ray diffraction of 3h	S13
5	Computational Studies	S15
6	Characterizations of substrates and products	S28
	6. 1 Characterizations of substrates	S29
	6. 2 Characterizations of products	S49
	Supplementary references	S73
	Appendix: ^1H and ^{13}C NMR spectra for new compounds	S74

5. Computational Studies

5.1 Computational methods

Density functional theory (DFT) calculations were performed using *Gaussian 16* rev. B.01 software,⁸ in the gas phase using the hybrid meta-GGA exchange-correlation functional M06-2X⁹ and the def2-SVP^{10,11} basis set for all atoms. The M06-2X functional⁹ was chosen as it gives the best agreement with the experimental redox potential values amongst 8 functionals tested for the study of computational redox potential calculations.¹² In addition, in a study of both experimental and computational electrochemical potentials for over 180 organic substrates, M06-2X functional gives an R^2 value of 0.97 for the correlation between the experimental and calculated redox potentials,¹³ implying that M06-2X functional performs well for studying organic radical species. In our previous study on the photocatalytic direct para-selective C-H amination of benzyl alcohols, this methodology has performed well in elucidating the catalytic mechanism and giving good agreement with experimental results.¹⁴

For radical systems and the openshell singlet system, the DFT calculations were performed within the unrestricted formalism using the unrestricted Kohn-Sham (UKS) theory. Furthermore, for the openshell singlet diradical systems involved in the radical-radical coupling step, the keyword “guess=mix” was used to ensure that unrestricted Hartree-Fock (UHF) wavefunction for singlet state (symmetry-broken solution) is used. The keyword “stable=opt” was used to ensure that the resulting wavefunction is stable with respect to an unrestricted wavefunction, as we expect the radical-radical coupling transition structure to possess significant diradical character.

Minima and transition structures on the potential energy surface (PES) were confirmed as such by harmonic frequency analysis, showing respectively zero and one imaginary frequency. Gibbs energies were evaluated at the reaction temperature of 25 °C and corrected for zero-point vibrational energies at the same level of theory, using Grimme’s scheme of quasi-RRHO treatment of vibrational entropies,¹⁵ using the GoodVibes code.¹⁶ Vibrational entropies of frequencies below 100 cm^{-1} were obtained according to a free rotor description, using a smooth damping function to interpolate between the

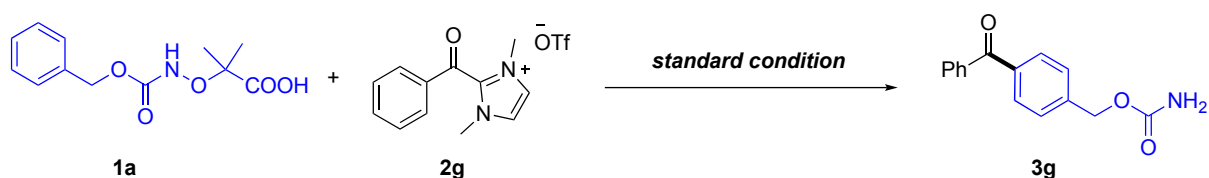
two limiting descriptions.¹⁵ The free energies reported in *Gaussian* from gas-phase optimization were further corrected using standard concentration of 1 mol/L,¹⁷ which were used in solvation calculations, instead of the gas-phase 1 atm used by default in the *Gaussian* program.

To improve on the accuracy of the corrected Gibbs energy profile, single point (SP) calculations on the gas phase M06-2X/def2-SVP optimized geometries were performed at M06-2X with def2-TZVP^{10,18} basis set for all atoms in the implicit SMD continuum solvation model¹⁹ for chloroform solvent (used to approximate PhCF₃, which is not in the list of default solvents in *Gaussian* software but showed similar yields and reactivities, Table S2), to account for the effect of solvent on the potential energy surface. The final corrected Gibbs energy SMD(CHCl₃)-M06-2X/def2-TZVP//M06-2X/def2-SVP is used for discussion throughout. All Gibbs energy values in the text and figures are quoted in kcal mol⁻¹.

Spin density plots are visualized using an isosurface value of 0.005 au throughout. All molecular structures and plots were visualized using *PyMOL* software.²⁰

5.2 Model reaction

The model reaction used for studying the reaction mechanism is shown in Scheme S1.



Scheme S1. Model reaction used for studying the catalytic mechanism.

5.3 Regioselectivity and chemoselectivity

The radical-radical coupling is the regio-determining step of the catalytic transformation. The DFT optimized transition state (TS) structures are shown in Figure S3, with the Gibbs energy values given relative to the radical species **I-a**. In **TS2**, the radical-radical coupling occurs at the *para*-position of the spiro 1,4-cyclohexadiene intermediate **II-a** and carbon atom of the ketyl radical intermediate, **III** (bond distance of 2.71 Å). The –NH group forms hydrogen bonding interaction (bond distance of 2.05

Å) with the ketyl oxygen atom (Figure S3). On the other hand, in **TS2'**, intermediate **I-a** orientates differently, such that no hydrogen bonding is formed; this has a barrier that is 1.7 kcal mol⁻¹ higher than **TS2**, demonstrating the role of H bonding in stabilizing the transition state structure.

For the C–C radical coupling TSs at other positions (*ortho*- and *meta*-), we consider the TS with the orientation of **II-a** in such a way that H-bonding formation is favored (same orientation of **TS2** instead of **TS2'**). For radical coupling at *ortho*-positions, two distinct TSs are possible, with **TS2o1** that has a lower barrier than **TS2o2** by 0.9 kcal mol⁻¹ (Figure S3). Thus, the C–C coupling at the *para*-position (**TS2**) is favored over the *ortho*-position (**TS2o1** and **TS2o2**) by at least 7.8 kcal mol⁻¹, which indicates the preference for *para*- to *ortho*-position by a factor of > 520,000 : 1 using simple transition state theory as an estimate (Section 5.4). For radical coupling at *meta*-positions, again two distinct TSs are possible, with **TS2m1** that has a lower barrier than **TS2m2** by 1.6 kcal mol⁻¹ (Figure S3). Overall, the C–C coupling at the *para*-position (**TS2**) is favored over the *meta*-position (**TS2m1** and **TS2m2**) by at least 39.4 kcal mol⁻¹ ($7.6 \times 10^{28} : 1$), which indicates that the formation of radical coupled product at *meta*-position is almost impossible, this is due to the parallel spins⁷ at the *meta*-carbon of **I-a** and the carbon of ketyl radical before they react and the lack of spin at these positions (Figure S4) in the TS structure (resonance structure does not show radical at *meta*-position).

TS2	TS2'
$\Delta G^\ddagger = -9.2$	$\Delta G^\ddagger = -7.5$
TS2o1	TS2o2
$\Delta G^\ddagger = -1.4$	$\Delta G^\ddagger = -0.5$
TS2m1	TS2m2
$\Delta G^\ddagger = 30.2$	$\Delta G^\ddagger = 31.8$

Figure S3. DFT optimized structures for transition states (TSs) of the radical-radical coupling step. Bond distances are given in Å. Gibbs energy are relative to species **I-a** as reference.

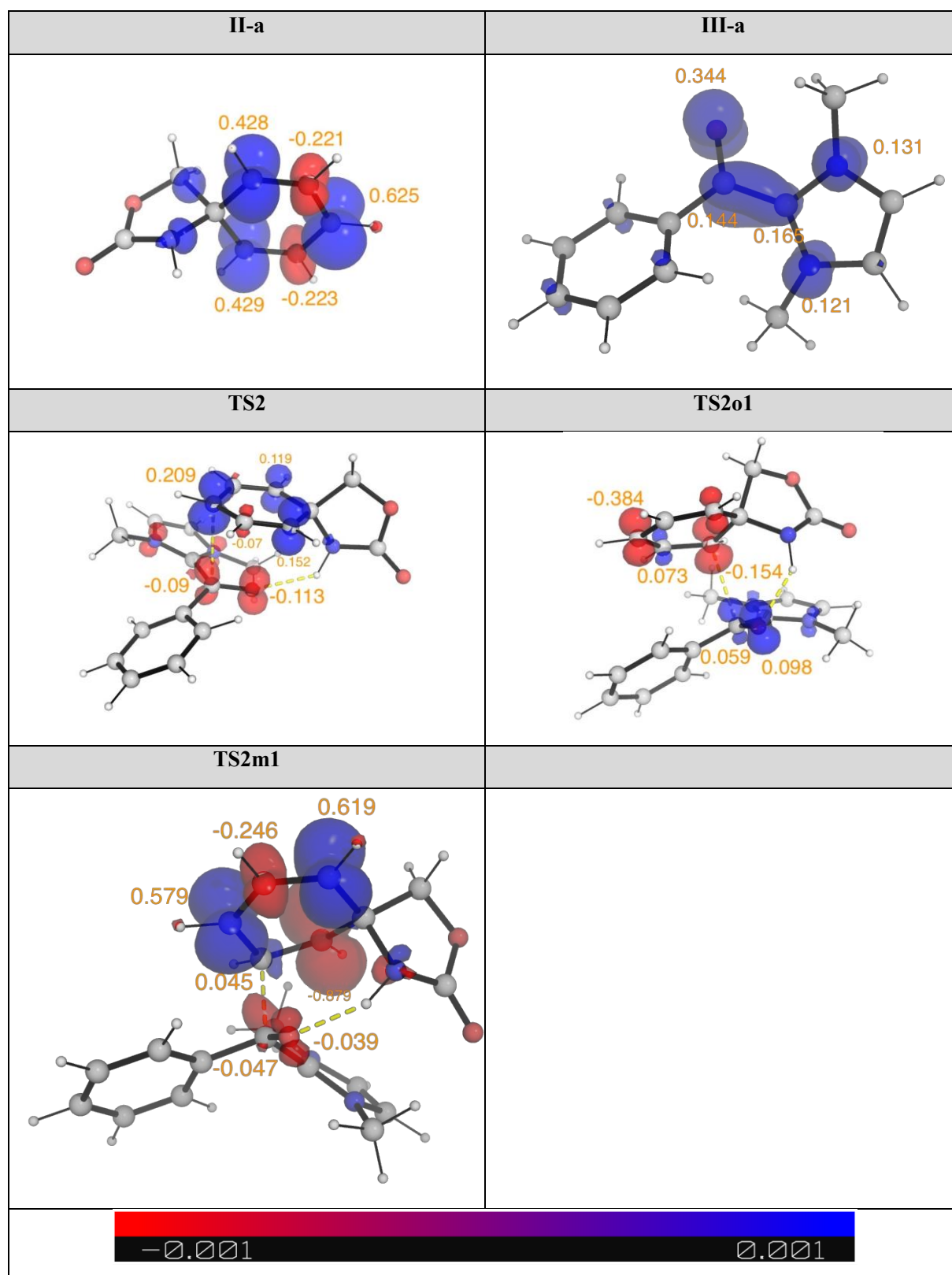


Figure S4. Spin density plots of selected species at an isosurface value of 0.005 au.

For chemoselectivity studies, we also consider the C–O coupling between the carbon

atom of **II-a** and the oxygen atom of ketyl radical **III-a**. Despite the more radical characteristic on oxygen atom than on carbon atom of ketyl radical **III-a**, the TS structures for C–O coupling has higher barriers than for the C–C coupling, as shown in Figure S5. The calculations indicate that the C–C coupling via TS2 has a barrier that is lower than C–O coupling (via either **TS2CO** or **TS2CO'** by 18.9 kcal mol⁻¹ (7.2×10^{13} : 1), thus only C–C coupled products will be observed.

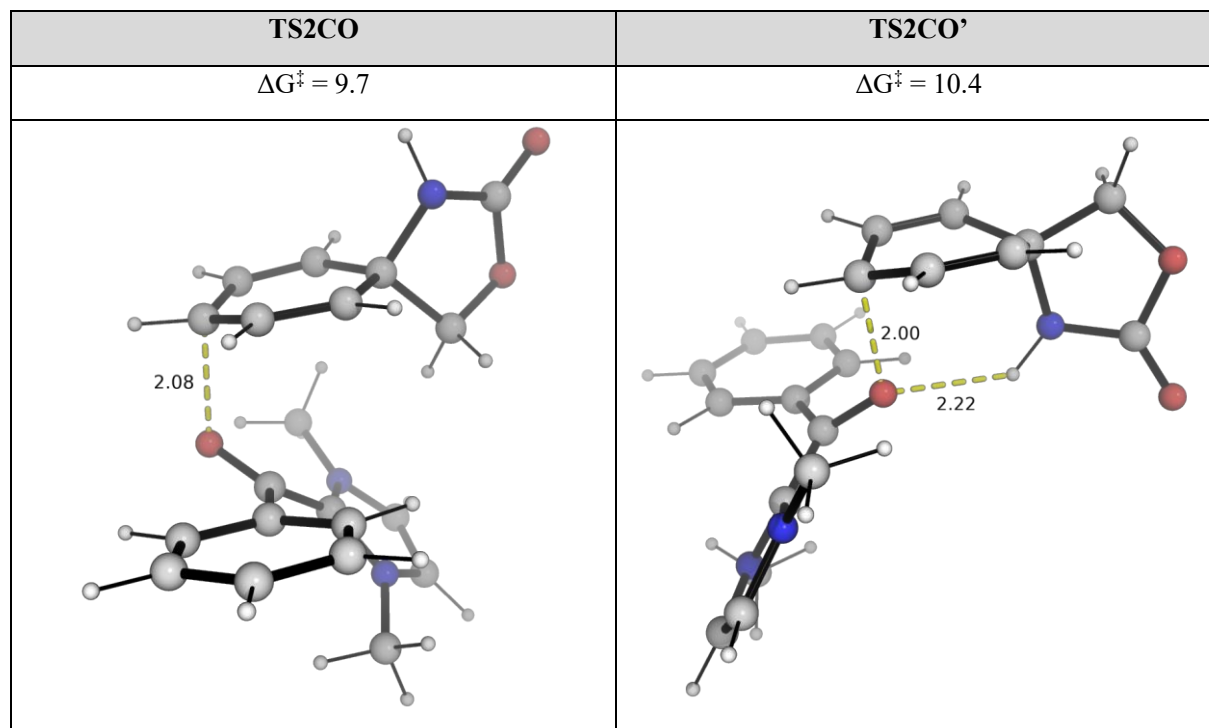


Figure S5. DFT optimized structures for transition states (TSs) of the radical-radical coupling step. Bond distances are given in Å. Gibbs energies are relative to species **I-a** as reference.

5.4 Determination of selectivity ratio using simple transition state theory

The Eyring equation

$$k = \frac{k_B T}{h} e^{-\Delta G^\ddagger / RT}$$

gives the rate constant under simple transition state theory (TST) assumptions.

Under kinetic control, as we compare the barrier heights difference between competing transition states, the product selectivity is given by:

$$\frac{k_A}{k_B} = \frac{e^{-\Delta G_A^\ddagger / RT}}{e^{-\Delta G_B^\ddagger / RT}} = e^{-\Delta \Delta G^\ddagger / RT}$$

where k_X is the rate constant of pathway X (X=A or B); ΔG_X^\ddagger is the activation barrier for pathway X; and $\Delta\Delta G_X^\ddagger$ is the difference in the barrier heights; and R is the gas constant, T the temperature. Note that the Eyring Equation pre-exponential factor cancels when comparing the ratio of the rate constants. Thus, for example, using the calculated $\Delta\Delta G_X^\ddagger$ value of 7.8 kcal/mol (difference of barrier heights between the **TS2** and **TS2o1**) at 25°C (298.15K), we obtained the selectivity ratio of about ~ 522,000 : 1.

5.5 Regioselectivity outcomes for substrates giving products **3y**, **3ad**, **3z**, **3ae**

To consider the effect of electron-withdrawing and electron donating groups on the regioselective outcome, we performed DFT calculations on the regioselectivity step for the substrates giving products **3y** and **3ad** (methoxy substitution at different positions) and **3z** and **3ae** (chlorine substitution at different positions).

From the Gibbs energy profile of the representative reaction (main text Figure 3), we see that the barrier for regioselective radical-radical coupling is between the spiro 1,4-cyclohexadiene intermediate **II-a** and the TS for the coupling (**TS2**). We focus on the spiro 1,4-cyclohexadiene intermediate for these products and identify the radical locations using spin density plots. These are shown in Figure S6.

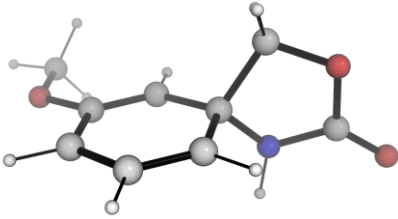
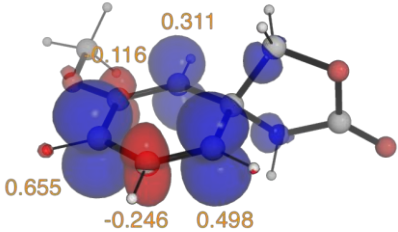
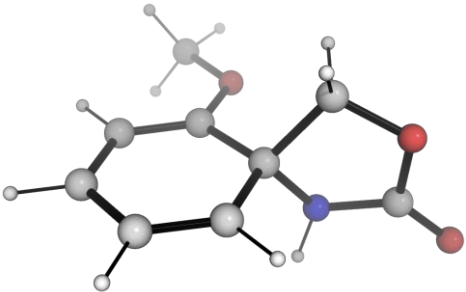
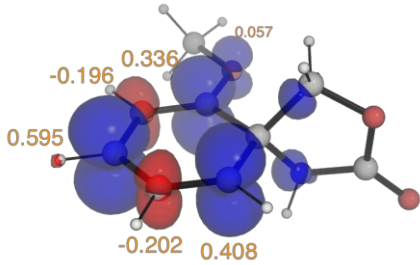
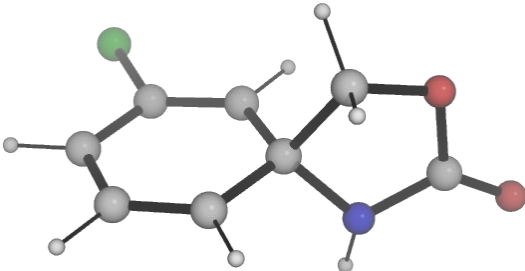
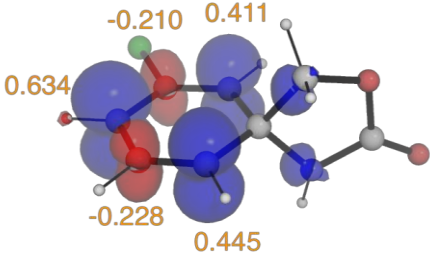
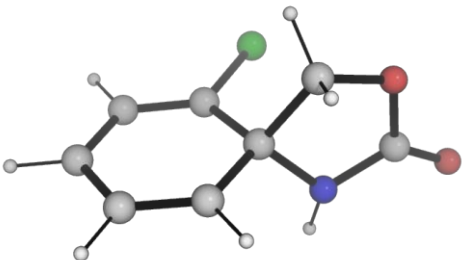
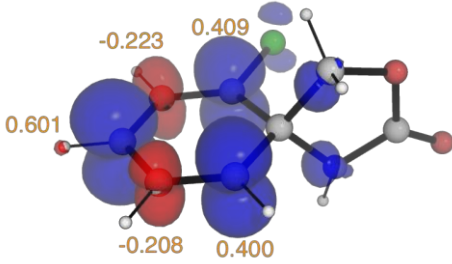
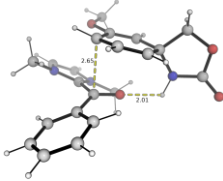
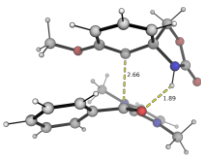
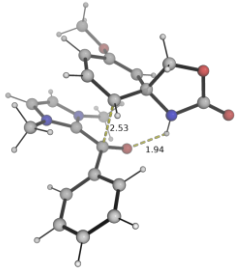
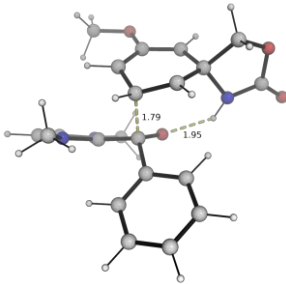
II-y (for product 3y)	
DFT structure	Spin density plot
	
II-ad (for product 3az)	
DFT structure	Spin density plot
	
II-z (for product 3z)	
DFT structure	Spin density plot
	
II-ae (for product 3ae)	
DFT structure	Spin density plot
	

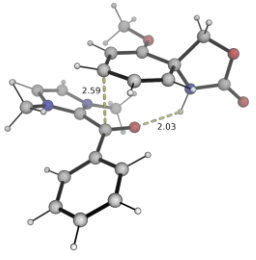
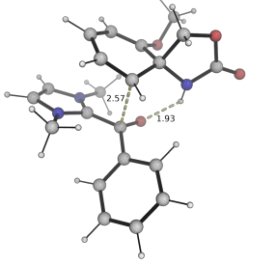
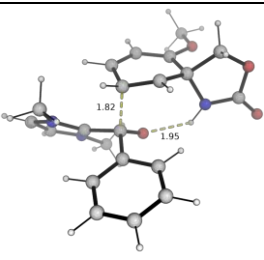
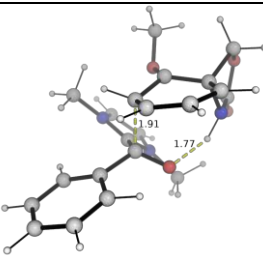
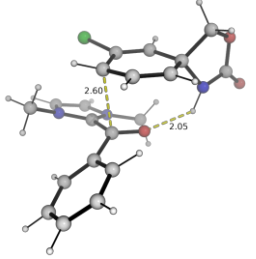
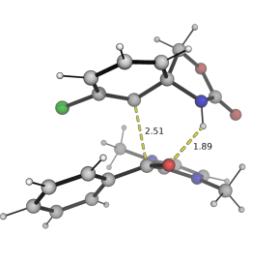
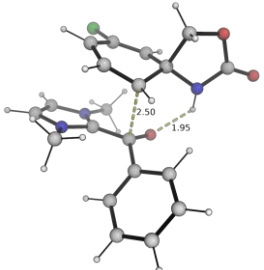
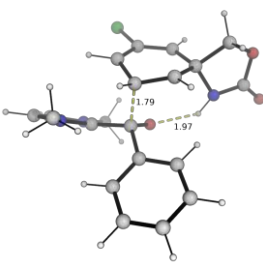
Figure S6. DFT-optimized structures and spin density plots of the spiro 1,4-cyclohexadiene intermediates leading to different products at an isosurface value of 0.005 au.

We note that the radical distributions (spin up/positive Mulliken spin density values and spin down/negative) in systems with both electron-donating group (methoxy in **3y** and **3ad**) at different positions (*ortho*- and *meta*- to spirocyclic carbon) and electron-withdrawing group (Cl in **3z** and **3ae**) at different positions (*ortho*- and *meta*- to spirocyclic carbon) are similar to the unsubstituted case (main text Figure 3c), except that the values vary. Moreover, the spin density has the largest value at the *para*-position, regardless of the substituent effects. This suggests that the radical localizations are independent of the substituent effects and that the radical-radical coupling will be favored at the *para*-position.

To fully discern the regioselectivity in these systems, we performed computational studies to locate the transition states of the regio-determining radical-radical coupling step for each substrate. All TSs could be located, except for the radical-radical coupling at the *para*-position for product **3y**. We note that this step may be barrierless (see Section 5.5.1) and thus used a structure close to the unsubstituted system to estimate its Gibbs energy. The DFT-optimized (except **TS2y-p-est**, where “est” denotes “estimated”) TS structures are shown in Figure S7.

From the results, we can see that regardless of whether the substituent is electron donating (e.g., methoxy group) or electron withdrawing (e.g., Cl group), at any position, either *ortho* or *meta* to the spirocyclic ipso carbon, the C–C coupling will occur selectively at the *para*-position.

TS2y (for product 3y)	
TS2y-p-est	TS2y-o1
$\Delta\Delta G^\ddagger = 0.0$	$\Delta G^\ddagger = 4.4$
	
TS2y-o2	TS2y-m
$\Delta G^\ddagger = 10.3$	$\Delta G^\ddagger = 42.8$
	
TS2ad (for product 3ad)	

TS2ad-p	TS2ad-o
$\Delta\Delta G^\ddagger = 0.0$	$\Delta G^\ddagger = 10.5$
	
TS2ad-m1	TS2ad-m2
$\Delta G^\ddagger = 38.4$	$\Delta G^\ddagger = 42.5$
	
TS2z(for product 3z)	
TS2z-p	TS2z-o1
$\Delta\Delta G^\ddagger = 0.0$	$\Delta G^\ddagger = 6.6$
	
TS2z-o2	TS2z-m
$\Delta G^\ddagger = 7.4$	$\Delta G^\ddagger = 42.0$
	
TS2ae(for product 3ae)	
TS2ae-p	TS2ae-o
$\Delta G^\ddagger = 0.0$	$\Delta G^\ddagger = 6.8$

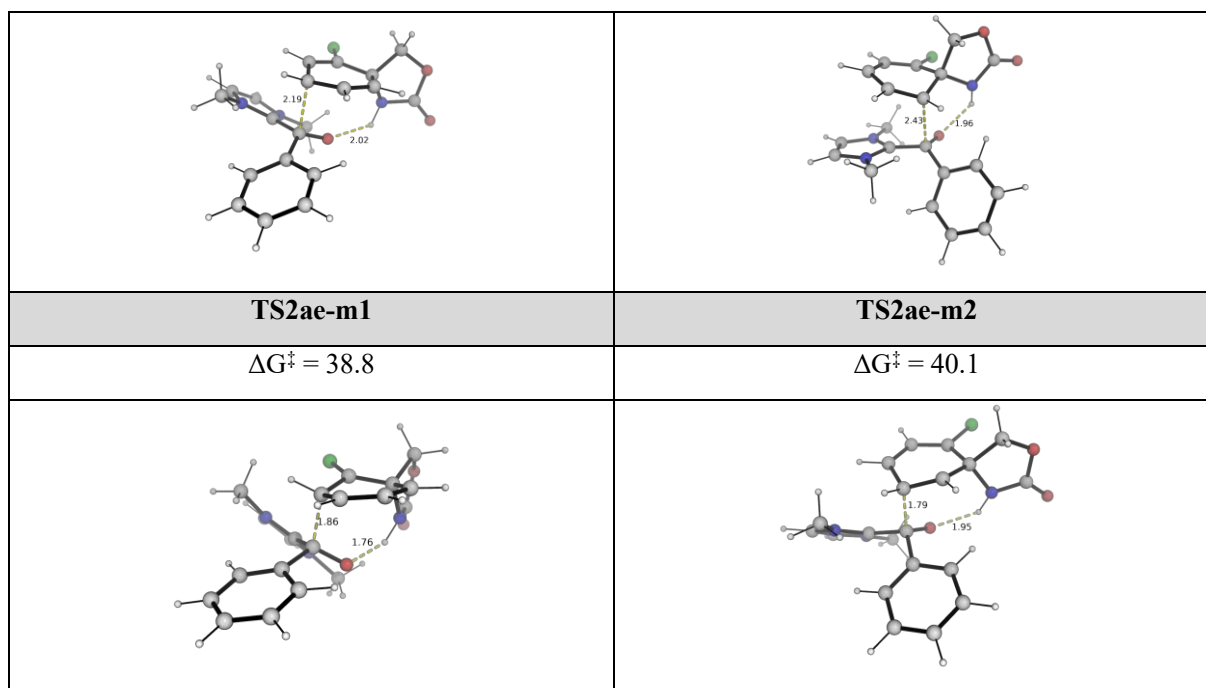


Figure S7. DFT optimized structures for transition states (TSs) of the radical-radical coupling step for substrates with substituents. Bond distances are given in Å. Relative Gibbs energies are taken with the lowest energy barrier TS (radical-radical coupling at *para*-position) as a reference for each system. In the structure names, “p” denotes *para*; “o” *ortho* and “m” *meta*.

5.5.1 Radical-radical coupling for product **3y** via TS2

Various methods (e.g., modifying the TS from the unsubstituted system followed by *modredudnant* job and TS search job; using QST2/3; relaxed PES scan then use the local maximum as guess structure etc) have been tried to locate this TS but to no avail. The relaxed PES scan shows that there may not be a transition state for the radical-radical coupling step at the *para*-position to yield product **3y** via TS2. The PES scan is shown in Figure S8.

We can see that from structure 1 to structure 5 in Figure S8 scanning along the C–C bond distance, there is no maximum energy, we have also used structure 4 and the ones adjacent to it as guess structures for TS search but to no avail. Moreover, subjecting structure 1 to direct geometry optimization gives the C–C coupling intermediate where the C–C bond is already formed, thus indicating that this step may be facile and does not have a transition state and may be barrierless.

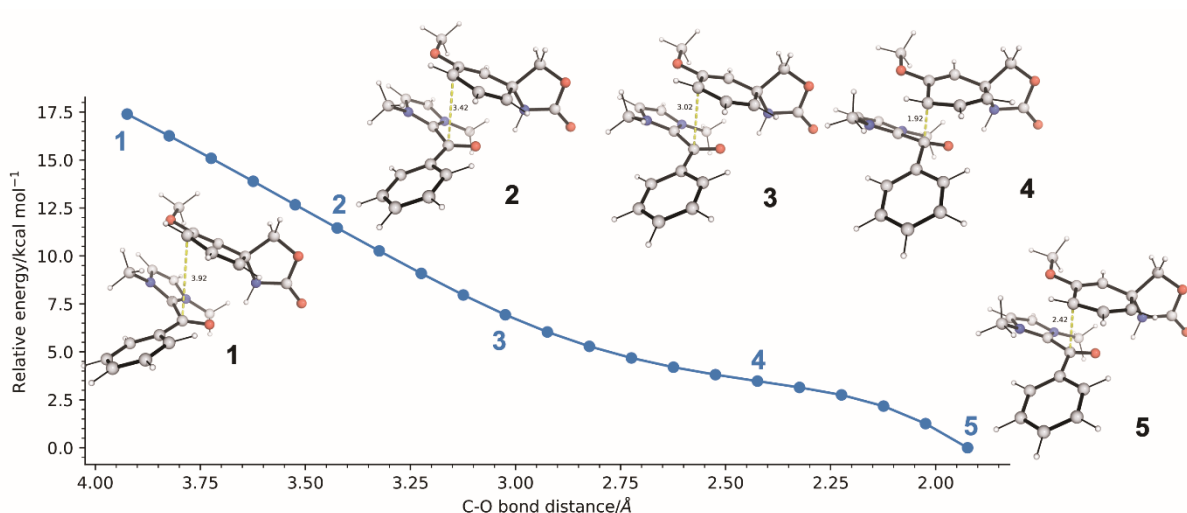


Figure S8. Relaxed PES scan along the C–C bond distance in the gas phase. Bond distances are given in Å.

5.6 Optimized DFT structures and absolute energies

Geometries of all optimized structures (in *.xyz* format with their associated gas-phase energy in Hartrees) are included in a separate folder named *DFT_optimized_structures*. All these data have been deposited and uploaded to <https://zenodo.org/records/13858725> (DOI: 10.5281/zenodo.13858725).

Absolute values (in Hartrees) for SCF energy, zero-point vibrational energy (ZPE), enthalpy and quasi-harmonic Gibbs free energy (at 25°C/298.15 K) for optimized structures are given below. Single point corrections in SMD chloroform using M06-2X/def2-TZVP level of theory are also included.

Table S5 Optimized structures and absolute energies, zero-point energies

Structure	E/au	ZPE/au	H/au	T.S/au	qh-G/au	SP SMD(CHCl ₃)- M06-2X/def2- TZVP
nhc	-304.434165	0.127837	-304.29846	0.035792	-304.334036	-304.7951512
I-a	-514.207638	0.148475	-514.04866	0.044725	-514.09169	-514.806563
TS1	-514.196553	0.148596	-514.03856	0.040818	-514.079093	-514.7979519
II-a	-514.233103	0.150395	-514.07321	0.041101	-514.113764	-514.831125
III-g	-649.032398	0.231174	-648.78698	0.051834	-648.837613	-649.777527
II-a_III-g	-	-	-	-	-	-
TS2	1163.293809	0.383752	-1162.8861	0.073546	-1162.95587	-1164.62638
IV-a	-	-	-	-	-	-
TS2	1163.292537	0.38487	-1162.8849	0.070072	-1162.952098	-1164.628457
IV-a	-	-	-	-	-	-
TS3	1163.303935	0.387063	-1162.8941	0.070574	-1162.961256	-1164.644281
TS3	-	-	-	-	-	-
TS3	1163.293442	0.385358	-1162.885	0.073044	-1162.953569	-1164.62729
nhc_V-a	-	-	-	-	-	-
nhc_V-a	1163.306873	0.384817	-1162.8976	0.077129	-1162.969413	-1164.641782
V-a	-858.851623	0.255724	-858.57996	0.057179	-858.634365	-859.8387633
3g	-858.886759	0.254892	-858.61496	0.059798	-858.671366	-859.8774133
TS2'	-	-	-	-	-	-
TS2'	1163.289004	0.385681	-1162.8806	0.06982	-1162.94764	-1164.626628
TS2o1	-	-	-	-	-	-
TS2o1	1163.286043	0.384719	-1162.8786	0.069325	-1162.945341	-1164.616327
TS2o2	-	-	-	-	-	-
TS2o2	1163.280613	0.384336	-1162.8735	0.069824	-1162.940529	-1164.614173
TS2m1	-	-	-	-	-	-
TS2m1	1163.235228	0.382909	-1162.8298	0.068406	-1162.895921	-1164.564532
TS2m2	-	-	-	-	-	-
TS2m2	1163.224797	0.38264	-1162.8193	0.070197	-1162.886431	-1164.560992
TS2CO'	-	-	-	-	-	-
TS2CO'	1163.262237	0.383585	-1162.8553	0.072944	-1162.92427	-1164.594816
TS2CO	-	-	-	-	-	-
TS2CO	1163.266426	0.384519	-1162.8588	0.071747	-1162.926854	-1164.597427
II-y	-628.626137	0.183498	-628.43066	0.046815	-628.476592	-629.3583737
TS2y-p-est	-	-	-	-	-	-
TS2y-p-est	1277.689512	0.419201	-1277.2447	0.075715	-1277.317308	-1279.157034
TS2y-o1	-	-	-	-	-	-
TS2y-o1	-	0.418099	-1277.2459	0.0738	-1277.317036	-1279.149917

	1277.689072					
	-					
TS2y-o2	1277.673341	0.418363	-1277.2299	0.074529	-1277.301333	-1279.140447
	-					
TS2y-m	1277.615451	0.415387	-1277.1746	0.076062	-1277.246867	-1279.08515
II-ad	-628.630964	0.184119	-628.43487	0.046929	-628.480732	-629.3620016
	-					
TS2ad-o	1277.673135	0.416888	-1277.2306	0.076812	-1277.303481	-1279.136295
	-					
TS2ad-m2	1277.628958	0.416941	-1277.1872	0.072961	-1277.257704	-1279.086838
TS2ad-p	-1277.68784	0.418438	-1277.2442	0.075231	-1277.316033	-1279.155125
TS2ad-m1	-1277.62205	0.416135	-1277.1805	0.076255	-1277.252778	-1279.091406
II-z	-973.679428	0.140661	-973.52807	0.044501	-973.571807	-974.435198
TS2z-m-est	-1622.67579	0.372988	-1622.2787	0.073363	-1622.348578	-1624.167172
	-					
TS2z-p	1622.747607	0.37609	-1622.3475	0.073155	-1622.417326	-1624.237184
	-					
TS2z-o1	1622.743642	0.376239	-1622.3437	0.071193	-1622.412417	-1624.227661
	-					
TS2z-o2	1622.736985	0.376094	-1622.3372	0.071717	-1622.40607	-1624.226073
II-ae	-973.684838	0.141123	-973.53307	0.044112	-973.576431	-974.4384049
	-					
TS2ae-o	1622.735616	0.376265	-1622.3356	0.071829	-1622.404541	-1624.227259
	-					
TS2ae-p	1622.749415	0.377148	-1622.3486	0.072181	-1622.4176	-1624.238877
	-					
TS2ae-m1	1622.692469	0.374509	-1622.2945	0.070755	-1622.362683	-1624.174989
TS2ae-m2	-1622.67895	0.37357	-1622.2814	0.073331	-1622.351066	-1624.171101

Supplementary references

1. H. Jiang, A. Studer, *Chem. Eur. J.* **2019**, *25*, 7105.
2. S. P. Morcillo, E. M. Dauncey, J. H. Kim, J. J. Douglas, N. S. Sheikh, D. Leonori, *Angew. Chem. Int. Ed.* **2018**, *57*, 12945.
3. a) J. L. Zhu, C. R. Schull, A. T. Tam, Á. R. Gómez, A. R. Gogoi, O. Gutierrez and K. A. Scheidt, *J. Am. Chem. Soc.* **2023**, *145*, 1535–1541; b) K. Scheidt, M. Rourke, C. Wang, C. Schull, *ChemRxiv.* **2022**.
4. D. SUN, C. Y. HU, and Y. YANG, *Asian. J. Chem*, **2014**, *15*, 4919-4920.
5. B. S. Bhatti, J. P. Strachan and W. S. Cadwell, *J. Org. Chem.* **2008**, *73*, 3497–3507.
6. B. Tan, N. Toda, and C. F. Barbas, *Angew. Chem. Int. Ed.* **2012**, *51*, 12538-12541.
7. a) A. V. Bay, K. P. Fitzpatrick, R. C. Betori, K. A. Scheidt, *Angew. Chem. Int. Ed.* **2020**, *59*, 9143; b) J. Zhuo, Y Zhang, Z Li and C Li. *ACS Catal.* **2020**, *10*, 3895–3903.
8. Frisch, M. J. .; Trucks, G. W. .; Schlegel, H. B. .; Scuseria, G. E. .; Robb, M. A. .; Cheeseman, J. R. .; Scalmani, G. .; Barone, V. .; Petersson, G. A. .; Nakatsuji, H. .; et al. Gaussian 16, Revision B.01. 2016.
9. Zhao, Y.; Truhlar, D. G. *Theor. Chem. Acc.* **2008**, *120* , 215–241.
10. Weigend, F.; Ahlrichs, R. *Phys. Chem. Chem. Phys.* **2005**, *7* (18), 3297–3305.
11. Weigend, F. *Phys. Chem. Chem. Phys.* **2006**, *8* , 1057–1065.
12. Zhang, X.; Paton, R. S. *Chem. Sci.* **2020**, *11* , 9309–9324.
13. Roth, H. G.; Romero, N. A.; Nicewicz, D. A.; Roth, H. G.; Romero, N. A.; Nicewicz, D. A.; Roth, H. G.; Romero, N. A.; Nicewicz, D. A. *Synlett* **2016**, *27*, 714–723.
14. Liu, D.; Tu, T.; Zhang, T.; Nie, G.; Liao, T.; Ren, S.-C.; Zhang, X.; Chi, Y. R. *Angew. Chem. Int. Ed.* **2024**, e202407293.
15. Grimme, S. *Chem: Eur. J.* **2012**, *18* (32), 9955–9964.
16. Luchini, G.; Alegre-Requena, J. V.; Funes-Ardoiz, I.; Paton, R. S. *FI000Research* **2020**, *9*, 291.
17. Bryantsev, V. S.; Diallo, M. S.; Goddard Iii, W. A.; Goddard, W. A. *J. Phys. Chem. B* **2008**, *112* (32), 9709–9719.
18. Hellweg, A.; Rappoport, D. *Phys. Chem. Chem. Phys.* **2014**, *17* (2), 1010–1017.
19. Marenich, A. V.; Cramer, C. J.; Truhlar, D. G. *J. Phys. Chem. B* **2009**, *113* (18), 6378–6396.
20. Schrödinger, L. *The PyMOL Molecular Graphics Development Component, Version 1.8*; 2015.